HOMOGENIZATION OF PLASMONIC CRYSTALS: SEEKING THE EPSILON-NEAR-ZERO EFFECT

MATTHIAS MAIER*, MARIOS MATTHEAKIS†, EFTHIMIOS KAXIRAS†‡, MITCHELL LUSKIN§, AND DIONISIOS MARGETIS¶

Abstract. By using an asymptotic analysis and numerical simulations, we derive and investigate a system of homogenized Maxwell's equations for conducting material sheets that are periodically arranged and embedded in a heterogeneous and anisotropic dielectric host. This structure is motivated by the need to design plasmonic crystals that enable the propagation of electromagnetic waves with no phase delay (epsilon-near-zero effect). Our microscopic model incorporates the surface conductivity of the two-dimensional (2D) material of each sheet and a corresponding line charge density through a line conductivity along possible edges of the sheets. Our analysis generalizes averaging principles inherent in previous Bloch-wave approaches. We investigate physical implications of our findings. In particular, we emphasize the role of the vector-valued corrector field, which expresses microscopic modes of surface waves on the 2D material. By using a Drude model for the surface conductivity of the sheet, we construct a Lorentzian function that describes the effective dielectric permittivity tensor of the plasmonic crystal as a function of frequency.

Key words. Homogenization, Asymptotic analysis, Maxwell's equations, Surface plasmon-polariton, Graphene, Plasmonic crystals

1. Introduction. The advent of two-dimensional (2D) materials with controllable electronic structures has opened up an unprecedented wealth of optical phenomena that challenge the classical diffraction limit of electromagnetic waves. Notable examples of related applications range from optical holography [36], tunable metamaterials [26], and cloaking [1], to subwavelength focusing lenses [9]. A striking feature of many of these applications is the possible emergence of an unusual regime with no refraction, referred to as epsilon-near-zero (ENZ) effect [21, 23, 13, 24, 33].

This effect calls for designing novel *plasmonic crystals* made of stacked metallic or semi-metallic 2D material structures arranged periodically with subwavelength spacing, and embedded in a dielectric host [21, 23, 20, 8]. The growing need to describe, engineer, and tune the optical properties of such plasmonic crystals motivates the present paper. To gain insight into their effective optical behavior, we utilize a homogenization procedure that systematically illuminates how such macroscopic properties emerge from the plasmonic microstructure.

In this paper, our key objectives are: (i) to elucidate how effective parameter values of plasmonic crystals are derived from asymptotics; and (ii) to investigate physical implications of the resulting, effective description. The homogenized system can be controlled by tuning (microscopic) geometry, (periodic) spacing, frequency, and conductivity of the 2D material. This description leads to precise conditions for the ENZ effect. Our work extends previous homogenization results for time-harmonic Maxwell's equations [20, 35, 2, 3, 12].

In particular, we carry out the following tasks:

– We introduce a microscopic model that incorporates the surface conductivity

*Department of Mathematics, Texas A&M University, College Station, TX 77843, USA.

†John A. Paulson School of Engineering and Applied Sciences, Harvard University, Cambridge, MA 02138, USA.

‡Department of Physics, Harvard University, Cambridge, MA 02138, USA.

§School of Mathematics, University of Minnesota, Minneapolis, MN 55455, USA.

¶Department of Mathematics, and Institute for Physical Science and Technology, and Center for Scientific Computation and Mathematical Modeling, University of Maryland, College Park, MD 20910, USA.

of 2D material sheets *and* a corresponding line charge density along possible edges of the sheets (see Section 2). The former may give rise to a *2D surface plasmon-polariton* (SPP) [22, 6] whereas the latter can cause an *edge plasmon-polariton* (EPP) [16, 10]. These waves are special fine-scale surface modes. The microscopic model describes a large class of plasmonic crystals consisting of periodic inclusions of metallic finite-size and curved 2D materials in a heterogeneous and anisotropic dielectric host (Sections 2, and 3).

- By using an asymptotic analysis, we derive a system of homogenized Maxwell's equations. This system features an effective permittivity tensor that results from an averaging procedure involving a vector-valued *corrector* field. This corrector is in turn described as a solution of a closed *cell problem* which encodes the microscopic details.
- We analytically demonstrate how the combination of the complex-valued surface conductivity of the sheets and the line conductivity along their edges can yield an ENZ effect (Section 4). In addition, by numerical simulations, we discuss the ENZ effect occurring in a few prototypical geometries consisting of nanoscale 2D structures. Furthermore, we present simulation results for the effective, macroscopic behavior of the corresponding electromagnetic fields (Section 5).
- By using a Drude model for the surface conductivity of the 2D material sheets, we construct a Lorentzian function that describes the effective dielectric permittivity tensor as a function of frequency for the prototypical geometries of our numerical study.

We discuss several physical implications of our findings. For instance, we identify the physical role of the corrector in our formulation: this field contains microscopic modes corresponding to waves on the 2D material. We show how the line charge density introduced in our microscopic model alters the ENZ effect of plasmonic crystals described previously [21, 23]. The Lorentzian function constructed for the effective dielectric permittivity tensor partly validates our results since its real and imaginary parts automatically satisfy the Kramers-Kronig relations.

1.1. Motivation: Epsilon-near-zero effect. Recently, 2D materials such as graphene and black phosphorus have been the subject of extensive experimental and theoretical studies. From the viewpoint of Maxwell's equations, the dielectric permittivity of a conducting 2D material may have a negative real part. As a result, SPPs of transverse-magnetic (TM) polarization may exist on the conducting sheet with a dispersion relation that allows for a transmitted wavenumber, k_{SPP}, much larger in magnitude than the free-space wavenumber, k_0 [18].

Specifically, for an infinite, flat conducting sheet in an isotropic and homogeneous ambient space, the SPP dispersion relation is [22]

$$\sqrt{k_0^2 - k_{\mathrm{SPP}}^2} = -\left(\frac{2k_0}{\omega\mu_0\sigma}\right) k_0,$$

where σ is the surface conductivity of the sheet, μ_0 is the magnetic permeability of the ambient space, and ω denotes the angular frequency. Note that $|k_{\mathrm{SPP}}| \gg k_0$ if $\mathrm{Im}\,\sigma > 0$ and $|\omega\mu_0\sigma| \ll k_0$ for an assumed $e^{-i\omega t}$ time dependence and lossless surrounding medium. Hence, the wavelength of the TM-polarized SPP scales linearly with σ if dissipation is relatively small ($0 < \mathrm{Re}\sigma \ll \mathrm{Im}\sigma$).

In general, the dispersion relation of transmitted waves through given 2D materials can be altered dramatically by introducing different geometries of the sheet, or different

arrangements of sheets in a dielectric host. In particular, plasmonic crystals are structures that consist of stacked, periodically aligned metallic layers. When the period is of the order of the SPP wavelength, unusual optical phenomena may occur, such as the ENZ effect and negative refraction [23, 19, 33, 24]. These properties can be precisely controlled by tuning the electronic structure of the 2D material, through chemical doping or other means, and the operating frequency, ω [37, 32].

The ENZ effect implies that at least one eigenvalue of the *effective* dielectric permittivity of the plasmonic structure is close to zero. This effect causes surprising optical features, which have not been obtained by traditional photonic systems. These features include decoupling of spatial and temporal field variations, tunneling through very narrow channels, constant phase transmission, strong field confinement, diffraction-free propagation, and ultrafast phase transitions [33, 28]. Many novel functional devices based on plasmonic crystals have been proposed, indicating the broad prospects of photonics based on the ENZ effect [23, 19, 33, 24, 28, 37].

Motivated by this perspective, in this paper we develop a general homogenization procedure for plasmonic crystals. In addition, we investigate the possibility for emergence of the ENZ effect in prototypical geometries with graphene layers, nanoribbons, and nanotubes.

1.2. Microscopic model and geometry. The geometry is shown in Figure 1. This consists of periodically stacked, possibly curved sheets, Σ^d, of a 2D material with surface conductivity $\sigma^d = d\,\sigma(\boldsymbol{x}, \boldsymbol{x}/d)$. We assume that a charge accumulation may occur via a *line conductivity*, $\lambda^d = d^2\,\lambda(\boldsymbol{x}, \boldsymbol{x}/d)$, on the edges $\partial\Sigma^d$ of the sheets. The sheets are embedded in a dielectric with *heterogeneous* permittivity $\varepsilon^d(\boldsymbol{x}) = \varepsilon(\boldsymbol{x}, \boldsymbol{x}/d)$ [35, 2, 12]. The functions ε, σ and λ depend on a slow scale, and are periodic and rapidly oscillating in a (fast) scale proportional to the *scaling parameter* d; typically, $d \ll 2\pi/k_0$.

At the microscale, we invoke time-harmonic Maxwell's equations for the electromagnetic field $(\boldsymbol{E}^d, \boldsymbol{H}^d)$ in domain Ω; see (2.1). The conductivities σ and λ are responsible for the induced current density $\boldsymbol{J}_{\Sigma^d} = \boldsymbol{\delta}_{\Sigma^d}\sigma^d\boldsymbol{E}^d + \boldsymbol{\delta}_{\partial\Sigma^d}\lambda^d\boldsymbol{E}^d$. This causes the following jump conditions on Σ^d:

$$\begin{cases} \left[\boldsymbol{\nu}\times\boldsymbol{E}^d\right]_{\Sigma^d} = 0\,, \quad \left[\boldsymbol{\nu}\times\boldsymbol{H}^d\right]_{\Sigma^d} = \sigma^d\boldsymbol{E}^d\,; \\ \left[\boldsymbol{\nu}\cdot(\varepsilon^d\boldsymbol{E}^d)\right]_{\Sigma^d} = \dfrac{1}{i\omega}\nabla\cdot(\sigma^d\boldsymbol{E}^d)\,, \quad \left[\boldsymbol{\nu}\cdot\boldsymbol{H}^d\right]_{\Sigma^d} = 0\,. \end{cases}$$

In addition, $\boldsymbol{J}_{\Sigma^d}$ causes corresponding (internal) boundary conditions on $\partial\Sigma^d\cap\Omega$, viz.,

$$\begin{cases} \left\{\boldsymbol{n}\times\boldsymbol{H}^d\right\}_{\partial\Sigma^d} = \lambda^d\boldsymbol{E}^d \quad \text{and} \\ \quad \boldsymbol{n}\cdot\left(\sigma^d\boldsymbol{E}^d\right) = \nabla\cdot\left(\lambda^d\boldsymbol{E}^d\right) \quad \text{on } \partial\Sigma^d\cap\Omega. \end{cases}$$

In the above, $[\,.\,]_{\Sigma^d}$ denotes the jump over Σ^d, $\boldsymbol{\nu}$ is the unit normal vector of the conducting sheets and $\boldsymbol{n}$ describes the outwards pointing unit normal vector on the edges, $\partial\Sigma^d$, orthogonal to $\boldsymbol{\nu}$. The symbol $\{\,.\,\}_{\partial\Sigma^d}$ denotes a respective jump over $\partial\Sigma^d$. A detailed discussion is given in Section 2.

1.3. Homogenized theory. We will demonstrate by a formal *asymptotic analysis* that in the case of scale separation, meaning if d is sufficiently small compared to the free-space wavelength, $2\pi/k_0$, the above problem manifesting the microstructure

can be expressed by the following *homogenized system*:

$$\begin{cases} \nabla \times \boldsymbol{\mathcal{E}} = i\omega\mu_0 \boldsymbol{\mathcal{H}}, \\ \nabla \times \boldsymbol{\mathcal{H}} = -i\omega\varepsilon^{\text{eff}} \boldsymbol{\mathcal{E}} + \boldsymbol{J}_a, \end{cases} \tag{1.1}$$

in which the dependence on (microscale) spacing d is eliminated. Here, $\boldsymbol{J}_a$ is a current source, and $(\boldsymbol{\mathcal{E}}, \boldsymbol{\mathcal{H}})$ describes an effective electromagnetic field subject to the *effective permittivity tensor*

$$\varepsilon_{ij}^{\text{eff}} := \int_Y \varepsilon(\boldsymbol{x},\boldsymbol{y})\big(\boldsymbol{e}_j + \nabla_y \chi_j(\boldsymbol{x},\boldsymbol{y})\big)\cdot \boldsymbol{e}_i \,\mathrm{d}y - \frac{1}{i\omega}\int_\Sigma \sigma(\boldsymbol{x},\boldsymbol{y})\big(\boldsymbol{e}_j + \nabla_y \chi_j(\boldsymbol{x},\boldsymbol{y})\big)\cdot \boldsymbol{e}_i \,\mathrm{d}o_y - \frac{1}{i\omega}\int_{\partial\Sigma} \lambda(\boldsymbol{x},\boldsymbol{y})\big(\boldsymbol{e}_j + \nabla_y \chi_j(\boldsymbol{x},\boldsymbol{y})\big)\cdot \boldsymbol{e}_i \,\mathrm{d}s.$$

In the above equation, Y denotes the unit cell with embedded boundary Σ whose edge is $\partial\Sigma$ (see Figure 1); $\boldsymbol{e}_i$ is the unit vector in the i-th direction; and $\nabla_y \boldsymbol{\chi}$ is the Jacobian of the *corrector*, $\boldsymbol{\chi}$, that solves the associated cell problem, cf. (3.8). A crucial property of ε^{eff} is that it manifests an interplay, and possible mutual cancellation, of three distinct averages. Thus, by tuning geometry, spacing, frequency and conductivities of the 2D material, we can force one or more eigenvalues of ε^{eff} to be close to zero. This ENZ effect is detailed in Section 4.

1.4. Past works. The derivation presented in this paper is based on a formal asymptotic analysis in the spirit of [5]. Note that in [20] a rigorous approach invoking two-scale convergence is applied to plasmonic crystals without a line charge density along edges. In the framework of homogenization theory for time-harmonic Maxwell's equations, we should also mention a number of other related, rigorous or formal, results [27, 35, 12, 2, 3]. In particular, in [12] a formal asymptotic analysis is applied to *finite* photonic crystals; and in [27] the authors homogenize Maxwell's equations in the presence of rough boundaries (see also [15]).

Broadly speaking, the design of structures with unusual optical properties is a highly active direction of research. For recent advances in photonics, we refer the reader to [14, 38]. In fact, the computation of effective material parameters in Maxwell's equations has a long history in physics and engineering. It is impossible to exhaustively list the related bibliography here. In regard to the homogenization of periodic and heterogeneous systems, we mention as examples [15, 31, 8, 17].

Notably, homogenization results for Maxwell's equations can be related to approaches based on *Bloch theory* for waves in periodic structures. In Section 4, we demonstrate that our homogenization result readily generalizes an averaging principle that was previously found in particular Bloch-wave solutions constructed for simple settings [21, 23]. In the context of layered structures usually only a few Bloch waves effectively contribute to the macroscopic field [34]. In contrast, our approach relies entirely on periodic upscaling principles and is thus *independent* of the choice of particular solutions. In fact, we derive effective equations and material parameters that are valid for a wide range of geometries without choosing any particular solutions *a priori*.

1.5. Limitations. Although the homogenization results presented in this paper are fairly general, our analysis bears limitations. We should mention the following issues:

- Our analysis leaves out *boundary effects* in the homogenization procedure due to the interaction of the microstructure (conducting sheet) with boundaries of

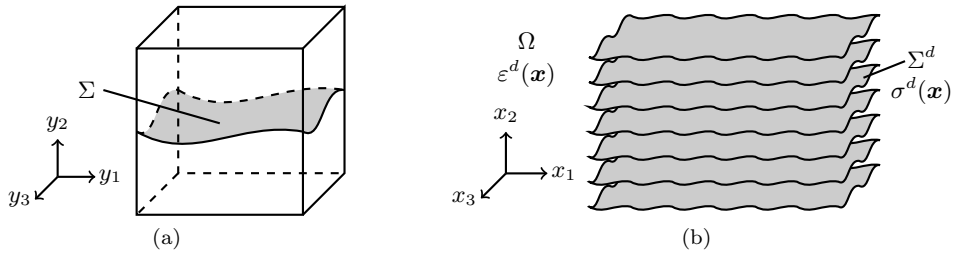

Fig. 1: Schematic of geometry. (a) The unit cell, $Y = [0,1]^3$, with microstructure Σ, a conducting sheet. (b) Computational domain Ω with rescaled periodic layers Σ^d and spatially dependent surface conductivity $\sigma^d(\boldsymbol{x})$. The ambient medium has a heterogeneous permittivity, $\varepsilon^d(\boldsymbol{x})$.

the domain. This simplification restricts the homogenization result either to layered microstructures immersed in a scattering domain, or to domains with periodic boundary conditions.

– Our asymptotic analysis relies on a strong periodicity assumption for the microstructure. Even though we allow material parameters to also depend on a slow scale, we do not account for a slowly varying geometry of the microstructure, i.e., the microscale elements (conducting sheets) form a strictly periodic structure in our treatment.
– We assume a scale separation between the free-space wavenumber, k_0, which we treat as of the order of unity ($k_0 \sim 1$), and the *SPP wavenumber*, k_{SPP}, with $k_{\mathrm{SPP}} \sim 1/d$. This assumption rules out resonance effects, if the period (spacing), d, is close to the free-space wavelength. In this vein, we do not discuss the case with resonant scaling, $k_{\mathrm{SPP}} \sim 1$.

1.6. Paper organization. The remainder of the paper is organized as follows. In Section 2, we introduce the microscale model and scaling assumptions. In Section 3, we derive a system of homogenized equations and the corresponding cell problem, which determine the effective material parameters. Section 4 provides a detailed discussion of the ENZ effect from our homogenization. In Section 5, we complement our analytical findings with computational results for the homogenized system in specific geometries. Section 6 concludes the paper with a summary of the key results and an outline of open problems. We use an $e^{-i\omega t}$ time dependence throughout. In the supplementary material, we provide detailed analytical derivations that are not essential for our paper.

2. Microscopic theory and geometry. In this section, we give a detailed description of the (full) microscale model and geometry. We also describe our scaling assumptions and discuss the rationale underlying them.

Our objective is to study Maxwell's equations in the (not necessarily bounded) domain $\Omega \subset \mathbb{R}^3$ that contains microstructures with periodically aligned, plasmonic hypersurfaces Σ^d; see Figure 1. These hypersurfaces are generated from the inscribed hypersurface Σ via scaling with a length scale, d, and periodically repeating a *unit cell*, $Y = [0,1]^3$. More precisely, we define

$$\Sigma^d = \big\{ d\,\boldsymbol{z} + d\,\boldsymbol{\varsigma} \;\; : \;\; \boldsymbol{z} \in \mathbb{Z}^3,\ \boldsymbol{\varsigma} \in \Sigma \big\},$$

where $\mathbb{Z}$ denotes the set of integers. Note that we make no specific assumption about

Σ, except that it is smooth (in Y and when periodically continued) so that it admits a well-defined surface normal. This property does neither imply that Σ has to be a connected manifold, nor that Σ has to have an intersection with the boundary of Y; see Section 5 for examples.

The relevant material parameters can be heterogeneous and tensor-valued. We assume that the ambient medium, which is contained in $\Omega \setminus \Sigma^d$, is described by a dielectric permittivity, $\varepsilon^d(\boldsymbol{x})$. Furthermore, the plasmonic sheets Σ^d have the associated surface conductivity $\sigma^d(\boldsymbol{x})$. In addition, we allow for a *line conductivity* $\lambda^d(\boldsymbol{x})$ on the edges, $\partial\Sigma^d$, of the sheets.

To derive a physically appealing homogenization limit, we assume that the spatial dependence of the material parameters can be separated into a slowly oscillating macroscale behavior and a (locally) periodic microscale behavior with structural period d [5, 30], viz.,

$$\varepsilon^d(\boldsymbol{x}) = \varepsilon\big(\boldsymbol{x}, \boldsymbol{x}/d\big), \qquad \sigma^d(\boldsymbol{x}) = d\,\sigma\big(\boldsymbol{x}, \boldsymbol{x}/d\big), \qquad \lambda^d(\boldsymbol{x}) = d^2\,\lambda\big(\boldsymbol{x}, \boldsymbol{x}/d\big)\ .$$

Here, $\varepsilon(\boldsymbol{x}, .)$, $\sigma(\boldsymbol{x}, .)$, and $\lambda(\boldsymbol{x}, .)$ are Y-periodic and tensor-valued, i.e., $\varepsilon\big(\boldsymbol{x}, \boldsymbol{y} + \boldsymbol{e}_i\big) = \varepsilon\big(\boldsymbol{x}, \boldsymbol{y}\big)$, $\sigma\big(\boldsymbol{x}, \boldsymbol{y} + \boldsymbol{e}_i\big) = \sigma\big(\boldsymbol{x}, \boldsymbol{y}\big)$, and $\lambda\big(\boldsymbol{x}, \boldsymbol{y} + \boldsymbol{e}_i\big) = \lambda\big(\boldsymbol{x}, \boldsymbol{y}\big)$, for any unit vector $\boldsymbol{e}_i$ and $\boldsymbol{x} \in \Omega$, $\boldsymbol{y} \in \mathbb{R}^3$.

The surface conductivity $\sigma(\boldsymbol{x}, \boldsymbol{y})$ deserves particular attention. This parameter describes the linear response of the (possibly curved) hypersurface Σ, or the conduction surface current on Σ, due to an incident electric field. In our modeling, we consider the matrix $\sigma(\boldsymbol{x}, \boldsymbol{y})$ to be rank deficient with a zero eigenvalue in the normal direction. More precisely, for a fixed choice $(\boldsymbol{x}, \boldsymbol{y})$ and for $\sigma(\boldsymbol{x}, \boldsymbol{y})$ described in local coordinates $(\boldsymbol{\tau}_1, \boldsymbol{\tau}_2, \boldsymbol{\nu})$, where $\boldsymbol{\nu}$ is the normal vector and $\boldsymbol{\tau}_i$ is an orthonormal tangential direction $(i = 1, 2)$, the conductivity tensor takes the form

$$\sigma^d \ = \ \begin{pmatrix} \sigma_{11} & \sigma_{12} & 0 \\ \sigma_{21} & \sigma_{22} & 0 \\ 0 & 0 & 0 \end{pmatrix}.$$

The rescaled surface conductivity, $\sigma^d(\boldsymbol{x}) = d\sigma\big(\boldsymbol{x}, \boldsymbol{x}/d\big)$, of the plasmonic sheets, Σ^d, is equally rank deficient with a zero eigenvalue in the normal direction on Σ^d.

We now turn our attention to the line conductivity, $\lambda^d(\boldsymbol{x}, \boldsymbol{y})$, of our model. In correspondence to σ^d, we assume that λ^d describes the linear response along the edges, $\partial\Sigma^d$, of Σ^d, or induced line current along $\partial\Sigma^d$, due to an incident electric field. This implies that the tensor $\lambda^d(\boldsymbol{x})$ is rank deficient with zero eigenvalues in directions perpendicular to the edge. More precisely, suppose we make a fixed choice $(\boldsymbol{x}, \boldsymbol{y})$ and let $\lambda(\boldsymbol{x}, \boldsymbol{y})$ be described in local coordinates $(\boldsymbol{\tau}_1, \boldsymbol{n}, \boldsymbol{\nu})$, where τ_1 lies along the edges $\partial\Sigma^d$, $\boldsymbol{\nu}$ is the normal on Σ^d, and $\boldsymbol{n}$ denotes the outward-pointing unit vector tangential to Σ^d and normal to its edges, $\partial\Sigma^d$. Accordingly, the tensor λ^d takes the form

$$\lambda^d \ = \ \begin{pmatrix} \lambda_{11} & 0 & 0 \\ 0 & 0 & 0 \\ 0 & 0 & 0 \end{pmatrix}.$$

Since we will apply a formal (heuristic) asymptotic analysis, our assumptions on the parameters are not too restrictive. Consequently, we use arbitrary tensor-valued functions ε and σ. A mathematically rigorous convergence result typically requires more restrictive assumptions [20].

2.1. On the scaling of conductivities. Our particular choice of scalings of the surface and line conductivities with d, viz.,

$$\sigma^d \sim d \ , \qquad \lambda^d \sim d^2 \ ,$$

deserves an explanation. Recall that the wavenumber, k_{SPP}, of the desired, fine-scale SPP on an infinite conducting sheet scales inversely proportional to the surface conductivity (Section 1). Hence, our choice of scaling of σ^d distinctly separates two scales: one related to the free-space wavenumber k_0 ($k_0 \sim 1$), determined by the average of ε^d, and another for the SPP wavenumber, $k_{\mathrm{SPP}} \sim 1/\sigma^d \sim 1/d$, on the conducting sheets [19]. By our scaling, the *interaction range* of the SPP on each sheet is of the order of d. More precisely, in the limit $d \to 0$ the strength with which SPPs on one sheet influence neighboring sheets remains constant. In addition, our choice of scaling implies that the total surface current on the sheets remains *finite*. In a similar vein we scale the line conductivity, λ^d, with d^2. In the limit $d \to 0$, this assumption yields a *finite* total line current on the edges of the conducting sheets.

It is worth mentioning that other scaling scenarios may lead to different homogenization results. For example, the assumption $\sigma^d \sim 1$ corresponds to a resonance which in turn yields an effective *permeability* tensor [7]. Such a configuration can exhibit a respective *mu-near-zero* effect. A variety of structures, e.g., nanorings, that exhibit a mu-near-zero effect are studied in [29].

2.2. Heterogeneous Maxwell's equations. The time-harmonic Maxwell equations for the electromagnetic field $(\boldsymbol{E}^d, \boldsymbol{H}^d)$ in $\Omega \setminus \Sigma^d$ are:

$$\begin{cases} \quad \nabla \times \boldsymbol{E}^d = i\omega\mu_0 \boldsymbol{H}^d \ , \quad \nabla \times \boldsymbol{H}^d = -i\omega\varepsilon^d \boldsymbol{E}^d + \boldsymbol{J}_a \ , \\ \nabla \cdot (\varepsilon^d \boldsymbol{E}^d) = \dfrac{1}{i\omega} \nabla \cdot \boldsymbol{J}_a \ , \quad \nabla \cdot \boldsymbol{H}^d = 0 \ . \end{cases} \tag{2.1}$$

The surface conductivity, σ^d, is responsible for the appearance of the current density $\boldsymbol{J}_{\Sigma^d} = \boldsymbol{\delta}_{\Sigma^d} \sigma^d \boldsymbol{E}^d$, on Σ^d. Accordingly, we must impose the following jump conditions on $\Sigma^d \cap \Omega \setminus \partial\Sigma^d$:

$$\begin{cases} \quad \Big[\boldsymbol{\nu} \times \boldsymbol{E}^d\Big]_{\Sigma^d} = 0 \ , & \Big[\boldsymbol{\nu} \times \boldsymbol{H}^d\Big]_{\Sigma^d} = \sigma^d \boldsymbol{E}^d \ , \\ \Big[\boldsymbol{\nu} \cdot (\varepsilon^d \boldsymbol{E}^d)\Big]_{\Sigma^d} = \dfrac{1}{i\omega} \nabla \cdot (\sigma^d \boldsymbol{E}^d) \ , & \Big[\boldsymbol{\nu} \cdot \boldsymbol{H}^d\Big]_{\Sigma^d} = 0 \ . \end{cases} \tag{2.2}$$

Here, $[\,.\,]_{\Sigma^d}$ denotes the jump over Σ^d with respect to a chosen normal $\boldsymbol{\nu}$, viz.,

$$[\boldsymbol{F}]_{\Sigma^d}(\boldsymbol{x}) := \lim_{\alpha \searrow 0} \Big(\boldsymbol{F}(\boldsymbol{x} + \alpha\boldsymbol{\nu}) - \boldsymbol{F}(\boldsymbol{x} - \alpha\boldsymbol{\nu}) \Big) \qquad \boldsymbol{x} \in \Sigma^d.$$

Equations (2.1) and (2.2) are supplemented with the following internal boundary conditions on the edges of the plasmonic sheets, Σ^d, due to the line conductivity λ^d:

$$\begin{cases} \Big\{ \boldsymbol{n} \times \boldsymbol{H}^d \Big\}_{\partial\Sigma^d} \ = \ \lambda^d \boldsymbol{E}^d, \\ \quad \boldsymbol{n} \cdot \big(\sigma^d \boldsymbol{E}^d\big) \ = \ \nabla \cdot \big(\lambda^d \boldsymbol{E}^d\big) \quad \text{on } \partial\Sigma^d \cap \Omega, \end{cases} \tag{2.3}$$

where $\boldsymbol{n}$ denotes the outward-pointing unit vector tangential to the 2D sheet Σ^d and normal to curve $\partial\Sigma^d$. In (2.3), the symbol $\{\,.\,\}_{\partial\Sigma^d}$ denotes a *singular* jump over the

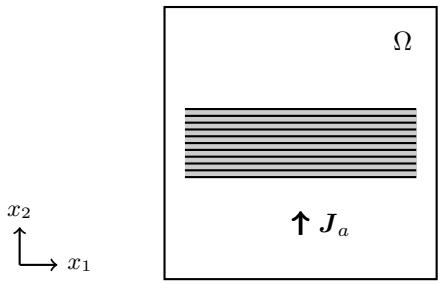

Fig. 2: Schematic of typical sheet configuration in our formalism. A Hertzian electric dipole, described by the current density $\boldsymbol{J}_a = \boldsymbol{J}_0\delta(\boldsymbol{x}-\boldsymbol{x}_0)$, is located below an array of sheets with microstructure, in the x_1x_2-plane. The rectangular domain Ω is equipped with absorbing boundary conditions at the top and bottom and periodic boundary conditions on the remaining sides.

edge, $\partial\Sigma^d$, viz.,

(2.4)
$$\{\boldsymbol{F}\}_{\partial\Sigma^d}(\boldsymbol{x}) := \lim_{\alpha\searrow 0}\int_{-\alpha}^{\alpha}\big(\boldsymbol{F}(\boldsymbol{x}+\alpha^2\boldsymbol{n}+\zeta\boldsymbol{\nu})-\boldsymbol{F}(\boldsymbol{x}-\alpha^2\boldsymbol{n}+\zeta\boldsymbol{\nu})\big)\,\mathrm{d}\zeta \qquad \boldsymbol{x}\in\partial\Sigma^d.$$

The jump condition in (2.3) stems from the property that, by virtue of the Ampère-Maxwell law, the line current $\lambda^d\boldsymbol{E}^d$ creates a *singular* magnetic field, $\boldsymbol{H}\sim(1/r)\,\boldsymbol{e}_\varphi$ as $r\to 0$, where r denotes the distance to the edge, $\partial\Sigma^d$, and $\boldsymbol{e}_\varphi$ is the unit vector in the azimuthal direction of the local cylindrical coordinate system. In this sense, jump (2.4) measures the strength of the singularity of the magnetic field $\boldsymbol{H}$ at any point $\boldsymbol{x}\in\partial\Sigma^d$. We refer the reader to Section SM1 of the supplementary material for a detailed discussion including a derivation of the jump $\{\,.\,\}_{\partial\Sigma^d}$.

The second compatibility condition in (2.3) is a direct consequence of charge conservation along the edges, $\partial\Sigma^d$, in view of the fact that σ^d vanishes identically outside the sheets. Let us explain. The *line charge accumulation* at the edges is related to the jump of the electric displacement field in the $\boldsymbol{n}$-direction over the edge, $\partial\Sigma^d$. This jump is in turn equal to $(i\omega)^{-1}\boldsymbol{n}\cdot\big(\sigma^d\boldsymbol{E}^d\big)$, since $\sigma^d\equiv 0$ outside Σ^d. The corresponding line charge density must be balanced by the divergence of the line current $\lambda^d\boldsymbol{E}^d$. Alternatively, compatibility conditions (2.3) can be derived from a variational formulation; see Section SM2 of the supplementary material.

Equations (2.1)–(2.3) form a closed system if they are complemented by suitable boundary conditions on $\partial\Omega$. We can impose either *absorbing* conditions, or *periodic* conditions, or, in the case with an unbounded domain, Ω, Silver-Müller radiation conditions at infinity [25, 22]. We make the important assumption that the domain, Ω, and the chosen boundary conditions on $\partial\Omega$ are compatible with the microstructure in the sense of the following simultaneous requirements:

- The microstructure is bounded, that is $\sigma(\boldsymbol{x},.)=0$ and $\varepsilon(\boldsymbol{x},.)=\varepsilon_0$ for $|\boldsymbol{x}|\geq C$ for some $C>0$.
- The microstructure only touches those parts of the boundary $\partial\Omega$ with periodic boundary conditions.

These requirements can ensure that the formal homogenization result derived in this paper remains valid everywhere. If any one of these requirements is not satisfied, a *boundary layer* might occur, which necessitates a special homogenization procedure

near $\partial\Omega$ [30]. In Figure 2, we show a typical sheet configuration and domain Ω that can be included in our formalism.

3. Two-scale expansions and asymptotics. In this section, we derive effective system (1.1) from microscale description (2.1) and (2.2), by means of a formal asymptotic analysis. For this purpose, consider the two-scale expansions [5, 30]

$$\boldsymbol{E}^d \to \boldsymbol{E}^{(0)}(\boldsymbol{x},\boldsymbol{y}) + d\boldsymbol{E}^{(1)}(\boldsymbol{x},\boldsymbol{y}) + d^2\boldsymbol{E}^{(2)}(\boldsymbol{x},\boldsymbol{y}) + \dots,$$
$$\boldsymbol{H}^d \to \boldsymbol{H}^{(0)}(\boldsymbol{x},\boldsymbol{y}) + d\boldsymbol{H}^{(1)}(\boldsymbol{x},\boldsymbol{y}) + d^2\boldsymbol{H}^{(2)}(\boldsymbol{x},\boldsymbol{y}) + \dots,$$

with the corresponding substitutions

$$\nabla \to \nabla_x + \frac{1}{d}\nabla_y, \qquad \varepsilon^d \to \varepsilon(\boldsymbol{x},\boldsymbol{y}), \qquad \sigma^d \to d\sigma(\boldsymbol{x},\boldsymbol{y}), \qquad \lambda^d \to d^2\lambda(\boldsymbol{x},\boldsymbol{y}).$$

Here, $\boldsymbol{y} \in Y$ denotes the fast variable, a now *independent* coordinate for the microscale. The small parameter, d, is treated as non-dimensional since it is scaled with $1/k_0$ which is set to unity.

The application of the above expansions to (2.1) and (2.2) and the subsequent dominant balance need to be carried out to the two lowest orders in the small parameter, d. This procedure results in eight equations and eight boundary conditions. By collecting all terms of the order of d^{-1} in region $\Omega \times Y$ and of the order of d^0 on $\Omega \times \Sigma$, we obtain the following set of equations:

$$\text{(3.1)} \qquad \begin{cases} \nabla_y \times \boldsymbol{E}^{(0)} = 0\ , & \nabla_y \times \boldsymbol{H}^{(0)} = 0\ , \\ \nabla_y \cdot (\varepsilon \boldsymbol{E}^{(0)}) = 0\ , & \nabla_y \cdot \boldsymbol{H}^{(0)} = 0\ ; \\ \left[\boldsymbol{\nu} \times \boldsymbol{E}^{(0)}\right]_\Sigma = 0\ , & \left[\boldsymbol{\nu} \times \boldsymbol{H}^{(0)}\right]_\Sigma = 0\ , \\ \left[\boldsymbol{\nu} \cdot (\varepsilon \boldsymbol{E}^{(0)})\right]_\Sigma = \dfrac{1}{i\omega}\nabla_y \cdot (\sigma \boldsymbol{E}^{(0)})\ , & \left[\boldsymbol{\nu} \cdot \boldsymbol{H}^{(0)}\right]_\Sigma = 0\ . \end{cases}$$

In a similar vein, the second set of equations is obtained by collecting all terms of the order of d^0 in $\Omega \times Y$ and of the order of d^1 on $\Omega \times \Sigma$, viz.,

$$\text{(3.2)} \qquad \begin{cases} \nabla_x \times \boldsymbol{H}^{(0)} + \nabla_y \times \boldsymbol{H}^{(1)} = -i\omega\varepsilon \boldsymbol{E}^{(0)} + \boldsymbol{J}_a\ , \\ \nabla_x \times \boldsymbol{E}^{(0)} + \nabla_y \times \boldsymbol{E}^{(1)} = i\omega\mu_0 \boldsymbol{H}^{(0)}\ , \\ \nabla_x \cdot (\varepsilon \boldsymbol{E}^{(0)}) + \nabla_y \cdot (\varepsilon \boldsymbol{E}^{(1)}) = \dfrac{1}{i\omega}\nabla_x \cdot \boldsymbol{J}_a\ , \quad \nabla_x \cdot \boldsymbol{H}^{(0)} + \nabla_y \cdot \boldsymbol{H}^{(1)} = 0\ , \end{cases}$$

and

$$\text{(3.3)} \qquad \begin{cases} \left[\boldsymbol{\nu} \times \boldsymbol{E}^{(1)}\right]_\Sigma = 0\ , \quad \left[\boldsymbol{\nu} \times \boldsymbol{H}^{(1)}\right]_\Sigma = \sigma \boldsymbol{E}^{(0)}\ , \\ \left[\boldsymbol{\nu} \cdot (\varepsilon \boldsymbol{E}^{(1)})\right]_\Sigma = \dfrac{1}{i\omega}\big(\nabla_x \cdot (\sigma \boldsymbol{E}^{(0)}) + \nabla_y \cdot (\sigma \boldsymbol{E}^{(1)})\big)\ , \quad \left[\boldsymbol{\nu} \cdot \boldsymbol{H}^{(1)}\right]_\Sigma = 0\ . \end{cases}$$

In (3.1)–(3.3), the differential equations are valid for $(\boldsymbol{x},\boldsymbol{y}) \in \Omega \times Y$; while the jump conditions hold for $(\boldsymbol{x},\boldsymbol{y}) \in \Omega \times \Sigma$.

So far, we used boundary conditions on the interior of the sheets, $\Sigma^d \cap \Omega \setminus \partial\Sigma^d$. We now focus on (2.3), imposed on the edges, $\partial\Sigma^d \cap \Omega$. First, we introduce the rescaled jump $\{\,.\,\}_{\partial\Sigma}$ in a way analogous to definition (2.4) for the jump $\{\,.\,\}_{\partial\Sigma^d}$, viz.,

$$\{\boldsymbol{F}\}_{\partial\Sigma}(\boldsymbol{x},\boldsymbol{y}) := \lim_{\alpha \searrow 0} \int_{-\alpha}^{\alpha} \big(\boldsymbol{F}(\boldsymbol{x},\boldsymbol{y} + \alpha^2\boldsymbol{n} + \zeta\boldsymbol{\nu}) - \boldsymbol{F}(\boldsymbol{x},\boldsymbol{y} - \alpha^2\boldsymbol{n} + \zeta\boldsymbol{\nu})\big)\,\mathrm{d}\zeta \quad \boldsymbol{y} \in \partial\Sigma.$$

By carrying out the leading-order asymptotic expansion for the singular jump (2.4), we see that $\{\,.\,\}_{\partial\Sigma^d} \to d\,\{\,.\,\}_{\partial\Sigma}$. Consequently, the first condition of (2.3) is expanded to

$$\Big\{\boldsymbol{n}\times\boldsymbol{H}^{(1)}\Big\}_{\partial\Sigma} \;=\; \lambda\boldsymbol{E}^{(0)} \quad \text{on } \Omega\times\big(\partial\Sigma\setminus\partial Y\big)\;. \tag{3.4}$$

Furthermore, the expansion of the second one of conditions (2.3) results in the following boundary conditions to the two lowest orders in d:

$$\boldsymbol{n}\cdot\big(\sigma\boldsymbol{E}^{(0)}\big) \;=\; \nabla_y\cdot\big(\lambda\boldsymbol{E}^{(0)}\big)\;,\qquad \boldsymbol{n}\cdot\big(\sigma\boldsymbol{E}^{(1)}\big) \;=\; \nabla_x\cdot\big(\lambda\boldsymbol{E}^{(0)}\big)+\nabla_y\cdot\big(\lambda\boldsymbol{E}^{(1)}\big)\;, \tag{3.5}$$

which hold on $\Omega\times\big(\partial\Sigma\setminus\partial Y\big)$.

We now use (3.1) to characterize $\boldsymbol{E}^{(0)}(\boldsymbol{x},\boldsymbol{y})$ and $\boldsymbol{H}^{(0)}(\boldsymbol{x},\boldsymbol{y})$ in more detail. Since a conservative periodic vector field is the sum of a constant vector and the gradient of a periodic function (potential), we can write the general solution to the first equation of (3.1) as (cf. [20])

$$\boldsymbol{E}^{(0)}(\boldsymbol{x},\boldsymbol{y}) = \boldsymbol{\mathcal{E}}(\boldsymbol{x})+\nabla_y\varphi(\boldsymbol{x},\boldsymbol{y})\;,\quad \varphi(\boldsymbol{x},\boldsymbol{y})=\sum_j \chi_j(\boldsymbol{x},\boldsymbol{y})\mathcal{E}_j(\boldsymbol{x})\;. \tag{3.6}$$

In this vein, a conservative and divergence-free periodic vector field must be constant. Hence, the general solution to the second and fourth laws of the first group of equations in (3.1) is given by

$$\boldsymbol{H}^{(0)}(\boldsymbol{x},\boldsymbol{y}) = \boldsymbol{\mathcal{H}}(\boldsymbol{x})\;. \tag{3.7}$$

The functions $\boldsymbol{\mathcal{E}}(\boldsymbol{x})$, $\boldsymbol{\mathcal{H}}(\boldsymbol{x})$ and $\chi_j(\boldsymbol{x},\boldsymbol{y})$ $(j=1,2,3)$ are further characterized below.

3.1. Derivation of cell problem. Next, we derive a closed set of equations that fully describe the functions $\chi_j(\boldsymbol{x},\boldsymbol{y})$ introduced in (3.6). These equations comprise the cell problem accounting for the microstructure details.

First, we substitute (3.6) into the respective, zeroth-order expressions in (3.1) and (3.5). Specifically, we use the third law of the first group of equations in (3.1); the first and third jump conditions in (3.1); and the first condition in (3.5). Thus, we obtain the following equations:

$$\begin{cases}
\displaystyle\sum_j \nabla_y\cdot\Big(\varepsilon(\boldsymbol{x},\boldsymbol{y})\big(\boldsymbol{e}_j+\nabla_y\chi_j(\boldsymbol{x},\boldsymbol{y})\big)\Big)\mathcal{E}_j(\boldsymbol{x}) \;=\; 0 \quad \text{in } \Omega\times Y\;,\\
\displaystyle\sum_j \Big[\boldsymbol{\nu}\times\Big(\varepsilon(\boldsymbol{x},\boldsymbol{y})\big(\boldsymbol{e}_j+\nabla_y\chi_j(\boldsymbol{x},\boldsymbol{y})\big)\Big)\Big]_\Sigma\,\mathcal{E}_j(\boldsymbol{x}) \;=\; 0 \quad \text{on } \Omega\times\Sigma\;,\\
\displaystyle\sum_j \Big[\boldsymbol{\nu}\cdot\Big(\varepsilon(\boldsymbol{x},\boldsymbol{y})\big(\boldsymbol{e}_j+\nabla_y\chi_j(\boldsymbol{x},\boldsymbol{y})\big)\Big)\Big]_\Sigma\,\mathcal{E}_j(\boldsymbol{x}) \;=\\
\qquad\displaystyle\frac{1}{i\omega}\sum_j \nabla_y\cdot\Big(\sigma(\boldsymbol{x},\boldsymbol{y})\big(\boldsymbol{e}_j+\nabla_y\chi_j(\boldsymbol{x},\boldsymbol{y})\big)\Big)\mathcal{E}_j(\boldsymbol{x}) \quad \text{on } \Omega\times\Sigma\;,\\
\displaystyle\sum_j \boldsymbol{n}\cdot\Big(\sigma(\boldsymbol{x},\boldsymbol{y})\big(\boldsymbol{e}_j+\nabla_y\chi_j(\boldsymbol{x},\boldsymbol{y})\big)\Big)\,\mathcal{E}_j(\boldsymbol{x}) \;=\\
\qquad\displaystyle\sum_j \nabla_y\cdot\Big(\lambda(\boldsymbol{x},\boldsymbol{y})\big(\boldsymbol{e}_j+\nabla_y\chi_j(\boldsymbol{x},\boldsymbol{y})\big)\Big)\mathcal{E}_j(\boldsymbol{x}) \quad \text{on } \Omega\times\big(\partial\Sigma\setminus\partial Y\big)\;.
\end{cases}$$

Here, $\mathcal{E}_j$ and χ_j are coupled. To simplify this description, we treat each term containing $\chi_j(\boldsymbol{x},\boldsymbol{y})$, which accounts for the microscale behavior of $\boldsymbol{E}^{(0)}(\boldsymbol{x},\boldsymbol{y})$, as independent from $\mathcal{E}_j(\boldsymbol{x})$ $(j=1,2,3)$. Thus, the above equations decouple into three distinct problems, one for each χ_j, viz.,

$$
\left\{
\begin{aligned}
\nabla_y \cdot \Big(\varepsilon(\boldsymbol{x},\boldsymbol{y})\big(\boldsymbol{e}_j + \nabla_y\chi_j(\boldsymbol{x},\boldsymbol{y})\big)\Big) &= 0 && \text{in } Y\setminus\Sigma\ ,\\
[\boldsymbol{\nu}\times(\boldsymbol{e}_j + \nabla_y\chi_j(\boldsymbol{x},\boldsymbol{y}))]_\Sigma &= 0 && \text{on } \Sigma\ ,\\
\Big[\boldsymbol{\nu}\cdot\Big(\varepsilon(\boldsymbol{x},\boldsymbol{y})\big(\boldsymbol{e}_j + \nabla_y\chi_j(\boldsymbol{x},\boldsymbol{y})\big)\Big)\Big]_\Sigma &= \\
\frac{1}{i\omega}\nabla_y\cdot\Big(\sigma(\boldsymbol{x},\boldsymbol{y})\big(\boldsymbol{e}_j + \nabla_y\chi_j(\boldsymbol{x},\boldsymbol{y})\big)\Big) && \text{on } \Sigma\ ,\\
\boldsymbol{n}\cdot\Big(\sigma(\boldsymbol{x},\boldsymbol{y})\big(\boldsymbol{e}_j + \nabla_y\chi_j(\boldsymbol{x},\boldsymbol{y})\big)\Big) &= \\
\nabla_y\cdot\Big(\lambda(\boldsymbol{x},\boldsymbol{y})\big(\boldsymbol{e}_j + \nabla_y\chi_j(\boldsymbol{x},\boldsymbol{y})\big)\Big) && \text{on } \partial\Sigma\setminus\partial Y\ .
\end{aligned}
\right. \tag{3.8}
$$

Equations (3.8) along with the condition that $\chi_j(\boldsymbol{x},\,.\,)$ be Y-periodic form the desired, closed cell problem. Notice that $\boldsymbol{x}$ plays the role of a parameter. Hence, the above cell problem uniquely describes $\chi_j(\boldsymbol{x},\,.\,)$ for any given (macroscopic) point $\boldsymbol{x}$ [20].

A remark on the two jump conditions in (3.8) is in order. The first jump condition ensures that the tangential part of $\boldsymbol{e}_j + \nabla_y\chi_j(\boldsymbol{x},\boldsymbol{y})$ on Σ is single valued. In regard to the second jump condition, recall that $\sigma(\boldsymbol{x},\boldsymbol{y})$ only acts on the tangential part of a vector field (to return a tangential vector). Thus, the right-hand side of the respective jump condition consists of the divergence of tangential field components, which in turn implies that this term is also single valued.

3.2. Homogenized macroscale problem. Our remaining task is to derive corresponding macroscale equations for the functions $\boldsymbol{\mathcal{E}}(\boldsymbol{x})$ and $\boldsymbol{\mathcal{H}}(\boldsymbol{x})$. We start by substituting (3.6) and (3.7) into the first equation of (3.2) and averaging (in cell Y) over the fast variable, $\boldsymbol{y}$. Hence, we obtain the following expression:

$$
\begin{aligned}
\nabla_x\times\boldsymbol{\mathcal{H}}(\boldsymbol{x}) + \int_Y \nabla_y\times\boldsymbol{H}^{(1)}(\boldsymbol{x},\boldsymbol{y})\,\mathrm{d}y = \\
-i\omega\sum_j\int_Y \varepsilon(\boldsymbol{x},\boldsymbol{y})\big(\boldsymbol{e}_j+\nabla_y\chi_j(\boldsymbol{x},\boldsymbol{y})\big)\,\mathrm{d}y\,\mathcal{E}_j(\boldsymbol{x}) + \boldsymbol{J}_a(\boldsymbol{x})\ .
\end{aligned}
\tag{3.9}
$$

By use of the Gauss theorem and the Y-periodicity of $\boldsymbol{H}^{(1)}$, the second term on the left-hand side of the above equation is written as

$$
\begin{aligned}
\int_Y \nabla_y\times\boldsymbol{H}^{(1)}\,\mathrm{d}y &= -\int_\Sigma\Big[\boldsymbol{\nu}\times\boldsymbol{H}^{(1)}\Big]_\Sigma\,\mathrm{d}o_y - \int_{\partial\Sigma\setminus\partial Y}\Big\{\boldsymbol{n}\times\boldsymbol{H}^{(1)}\Big\}_{\partial\Sigma^d}\,\mathrm{d}s\\
&= -\int_\Sigma\sigma(\boldsymbol{x},\boldsymbol{y})\boldsymbol{E}^{(0)}\,\mathrm{d}o_y - \int_{\partial\Sigma\setminus\partial Y}\lambda(\boldsymbol{x},\boldsymbol{y})\boldsymbol{E}^{(0)}\mathrm{d}s\\
&= -\sum_j\Bigg\{\int_\Sigma\sigma(\boldsymbol{x},\boldsymbol{y})\big(\boldsymbol{e}_j+\nabla_y\chi_j\big)\,\mathrm{d}o_y\\
&\qquad + \int_{\partial\Sigma\setminus Y}\lambda(\boldsymbol{x},\boldsymbol{y})\big(\boldsymbol{e}_j+\nabla_y\chi_j\big)\mathrm{d}s\Bigg\}\,\mathcal{E}_j(\boldsymbol{x})\ .
\end{aligned}
$$

In the above, the second equality comes from using the second jump condition of (3.3), and (3.4). The third equality follows from (3.6). Let us now define the *effective permittivity tensor* ε^{eff} by

(3.10)
$$\varepsilon^{\text{eff}}_{ij}(\boldsymbol{x}) := \int_Y \varepsilon(\boldsymbol{x},\boldsymbol{y})\big(\boldsymbol{e}_j+\nabla_y\chi_j(\boldsymbol{x},\boldsymbol{y})\big)\cdot\boldsymbol{e}_i\,\mathrm{d}y-\frac{1}{i\omega}\int_\Sigma \sigma(\boldsymbol{x},\boldsymbol{y})\big(\boldsymbol{e}_j+\nabla_y\chi_j(\boldsymbol{x},\boldsymbol{y})\big)\cdot\boldsymbol{e}_i\,\mathrm{d}o_y - \frac{1}{i\omega}\int_{\partial\Sigma\setminus\partial Y}\lambda(\boldsymbol{x},\boldsymbol{y})\big(\boldsymbol{e}_j+\nabla_y\chi_j(\boldsymbol{x},\boldsymbol{y})\big)\cdot\boldsymbol{e}_i\,\mathrm{d}s\ .$$

In view of this definition of ε^{eff}, (3.9) takes the form

$$\nabla\times\boldsymbol{\mathcal{H}} = -i\omega\varepsilon^{\text{eff}}\boldsymbol{\mathcal{E}}+\boldsymbol{J}_a\ ,$$

which describes the effective Ampére-Maxwell law.

The last three equations of (3.2) can be manipulated in a similar fashion. For example, consider the third equation. By using (3.6) and (3.7) and averaging over the fast variable, $\boldsymbol{y}$, we obtain

$$\nabla_x\cdot\Big(\sum_j\int_Y\varepsilon(\boldsymbol{x},\boldsymbol{y})\big(\boldsymbol{e}_j+\nabla_y\chi_j(\boldsymbol{x},\boldsymbol{y})\big)\,\mathrm{d}y\,\mathcal{E}_j(\boldsymbol{x})\Big) + \int_Y\nabla_y\cdot\big(\varepsilon(\boldsymbol{x},\boldsymbol{y})\boldsymbol{E}^{(1)}(\boldsymbol{x},\boldsymbol{y})\big)\,\mathrm{d}y=\frac{1}{i\omega}\nabla_x\cdot\boldsymbol{J}_a(\boldsymbol{x})\ . \tag{3.11}$$

Next, we manipulate the second term of the left-hand side by applying the Gauss theorem and utilizing the second jump condition of (3.3), as follows:

$$\begin{aligned}\int_Y\nabla_y\cdot(\varepsilon\boldsymbol{E}^{(1)})\,\mathrm{d}y &= -\int_\Sigma\big[\nu\cdot(\varepsilon\boldsymbol{E}^{(1)})\big]_\Sigma\,\mathrm{d}o_y\\ &= -\int_\Sigma\frac{1}{i\omega}\big(\nabla_x\cdot(\sigma\boldsymbol{E}^{(0)})+\nabla_y\cdot(\sigma\boldsymbol{E}^{(1)})\big)\,\mathrm{d}o_y\\ &= -\frac{1}{i\omega}\nabla_x\cdot\Big(\sum_j\int_\Sigma\sigma(\boldsymbol{x},\boldsymbol{y})\big(\boldsymbol{e}_j+\nabla_y\chi_j(\boldsymbol{x},\boldsymbol{y})\big)\,\mathrm{d}o_y\,\mathcal{E}_j(\boldsymbol{x})\,\mathrm{d}o_y\Big)\\ &\qquad -\frac{1}{i\omega}\int_\Sigma\nabla_y\cdot(\sigma\boldsymbol{E}^{(1)})\,\mathrm{d}o_y\ .\end{aligned}$$

By applying the Gauss theorem and utilizing the second boundary condition in (3.5), we find

$$\begin{aligned}\int_\Sigma\nabla_y\cdot(\sigma\boldsymbol{E}^{(1)})\,\mathrm{d}o_y &= \int_{\partial\Sigma}\boldsymbol{n}\cdot\big(\sigma\boldsymbol{E}^{(1)}\big)\,\mathrm{d}s = \int_{\partial\Sigma\setminus\partial Y}\boldsymbol{n}\cdot\big(\sigma\boldsymbol{E}^{(1)}\big)\,\mathrm{d}s\\ &= \int_{\partial\Sigma\setminus\partial Y}\nabla_x\cdot(\lambda\boldsymbol{E}^0)+\nabla_y\cdot(\lambda\boldsymbol{E}^1)\,\mathrm{d}s\\ &= \nabla_x\cdot\left(\sum_j\int_{\partial\Sigma\setminus\partial Y}\lambda(\boldsymbol{x},\boldsymbol{y})\big(\boldsymbol{e}_j+\nabla_y\chi_j(\boldsymbol{x},\boldsymbol{y})\big)\,\mathrm{d}s\,\boldsymbol{\mathcal{E}}_j(\boldsymbol{x})\right)\ .\end{aligned}$$

The second equality (exclusion of ∂Y) exploits the fact that $\sigma\boldsymbol{E}^{(1)}(\boldsymbol{x},.)$ is Y-periodic and, thus, single valued on $\partial\Sigma\cap\partial Y$. Notice, however, that the normal vector $\boldsymbol{n}$ changes

sign. The last integral in the second line vanishes because $\partial\Sigma \setminus Y$ has no boundary. Substituting the result of these manipulations into (3.11) and utilizing (3.10), we obtain

$$\nabla \cdot (\varepsilon^{\text{eff}} \boldsymbol{\mathcal{E}}) = \frac{1}{i\omega} \nabla \cdot \boldsymbol{J}_a .$$

Similar steps can be applied to the remaining equations of (3.2). The homogenized system is

$$\left\{ \begin{array}{l} \nabla \times \boldsymbol{\mathcal{E}} = i\omega\mu_0 \boldsymbol{\mathcal{H}} \ , \quad \nabla \times \boldsymbol{\mathcal{H}} = -i\omega\varepsilon^{\text{eff}} \boldsymbol{\mathcal{E}} + \boldsymbol{J}_a \ ; \\ \nabla \cdot (\varepsilon^{\text{eff}} \boldsymbol{\mathcal{E}}) = \dfrac{1}{i\omega} \nabla \cdot \boldsymbol{J}_a \ , \quad \nabla \cdot \boldsymbol{\mathcal{H}} = 0 \ . \end{array} \right. \tag{3.12}$$

4. Epsilon-near-zero effect. A crucial feature of the averaging for the effective permittivity, $\varepsilon^{\text{eff}}(\boldsymbol{x})$, as implied by (3.10), is the *interplay* of three distinct averages: one for the bulk permittivity, ε; another for the surface conductivity, σ; and a third one for the line conductivity, λ. Each of these averages has a positive real part. This interplay can be exploited as follows. By tuning the microscopic geometry, periodic spacing, frequency, or surface or line conductivity, we can in principle force at least one eigenvalue of $\varepsilon^{\text{eff}}(\boldsymbol{x})$ to be close to zero. In the case with an $\boldsymbol{x}$-independent ε^{eff}, this condition amounts to the ENZ effect in the direction of propagation determined by the respective eigenvector(s) [21, 23].

In the remainder of this section, we discuss the simplified case with a vanishing corrector, $\boldsymbol{\chi}$. In this case, we derive an explicit formula for the special spacing, $d = d_c$, called the critical spacing, that implies the ENZ effect in the presence of the line conductivity, λ. We show how our present averaging procedure is related to results of a Bloch-wave approach [21]. Lastly, we discuss in some detail the character and physical role of the corrector, $\boldsymbol{\chi}$.

4.1. Case with vanishing corrector $\boldsymbol{\chi}$: Formalism. In general, the corrector, $\boldsymbol{\chi}$, implicitly depends on the geometry and material parameters such as σ and λ. Accordingly, the derivation of closed, analytical formulas for $\boldsymbol{\chi}$ may be possible only in a limited number of situations. We now restrict attention to the particular yet physically appealing case with a vanishing corrector, $\boldsymbol{\chi}$. Our goal is to better understand the emerging ENZ effect.

Technically speaking, the solution, $\boldsymbol{\chi}$, of cell problem (3.8) vanishes whenever the forcing term in this problem is identically zero. This term may not be immediately obvious by inspection of (3.8). In order to gain some insight into its character, we invoke the weak formulation of the cell problem. To this end, we multiply the first equation in (3.8) with a smooth and Y-periodic test function, ψ, and integrate over Y (see also Section SM2 of the supplementary material). Two subsequent integrations by parts, and use of the requisite jump and boundary conditions, yield

$$\begin{aligned} 0 \ = \ & \int_Y \varepsilon(\boldsymbol{x},\boldsymbol{y}) \big(\boldsymbol{e}_j + \nabla_y \chi_j(\boldsymbol{x},\boldsymbol{y})\big) \cdot \nabla_y \psi(\boldsymbol{y}) \ \mathrm{d}y \\ & - \frac{1}{i\omega} \int_\Sigma \sigma(\boldsymbol{x},\boldsymbol{y}) \big(\boldsymbol{e}_j + \nabla_y \chi_j(\boldsymbol{x},\boldsymbol{y})\big) \cdot \nabla_y \psi(\boldsymbol{y}) \ \mathrm{d}o_y \\ & - \frac{1}{i\omega} \int_{\partial\Sigma \setminus \partial Y} \lambda(\boldsymbol{x},\boldsymbol{y}) \big(\boldsymbol{e}_j + \nabla_y \chi_j(\boldsymbol{x},\boldsymbol{y})\big) \cdot \nabla_y \psi(\boldsymbol{y}) \, \mathrm{d}s \ . \end{aligned}$$

The forcing term corresponds to the following term:

$$\int_Y \varepsilon(\boldsymbol{x},\boldsymbol{y})\,\boldsymbol{e}_j\cdot\nabla_y\psi(\boldsymbol{y})\;\mathrm{d}y-\frac{1}{i\omega}\int_\Sigma \sigma(\boldsymbol{x},\boldsymbol{y})\,\boldsymbol{e}_j\cdot\nabla_y\psi(\boldsymbol{y})\;\mathrm{d}o_y - \frac{1}{i\omega}\int_{\partial\Sigma\setminus\partial Y}\lambda(\boldsymbol{x},\boldsymbol{y})\,\boldsymbol{e}_j\cdot\nabla_y\psi(\boldsymbol{y})\,\mathrm{d}s\;. \tag{4.1}$$

Thus, the requirement of having a vanishing corrector means that (4.1) must vanish identically for every possible choice of ψ. One more integration by parts converts expression (4.1) to

$$i\omega\int_Y \nabla_y\cdot\big(\varepsilon(\boldsymbol{x},\boldsymbol{y})\boldsymbol{e}_j\big)\psi(\boldsymbol{y})\;\mathrm{d}y+\int_{\partial\Sigma}\boldsymbol{n}\cdot\big(\sigma(\boldsymbol{x},\boldsymbol{y})\boldsymbol{e}_j\big)\psi(\boldsymbol{y})\,\mathrm{d}s - \int_\Sigma \nabla_y\cdot\big(\sigma(\boldsymbol{x},\boldsymbol{y})\boldsymbol{e}_j\big)\psi(\boldsymbol{y})\;\mathrm{d}o_y-\int_{\partial\Sigma\setminus\partial Y}\nabla_y\cdot\big(\lambda(\boldsymbol{x},\boldsymbol{y})\boldsymbol{e}_j\big)\psi(\boldsymbol{y})\,\mathrm{d}s\;.$$

Thus, the forcing is necessarily zero whenever the following conditions hold simultaneously:

$$\begin{cases} \nabla_y\cdot\varepsilon(\boldsymbol{x},\boldsymbol{y}) \;=\; 0 & \text{in } Y\;,\\ \nabla_y\cdot\sigma(\boldsymbol{x},\boldsymbol{y}) \;=\; 0 & \text{on } \Sigma\;,\\ \boldsymbol{n}\cdot\sigma(\boldsymbol{x},\boldsymbol{y})-\nabla_y\cdot\lambda(\boldsymbol{x},\boldsymbol{y}) \;=\; 0 & \text{on } \partial\Sigma\setminus\partial Y\;. \end{cases} \tag{4.2}$$

Note that σ and λ encode information about the curvature of Σ and $\partial\Sigma$, respectively. This implies that for a non-flat surface Σ, or for a surface with (arbitrarily shaped) internal edges, $\sigma(\boldsymbol{x},\boldsymbol{y})$ and $\lambda(\boldsymbol{x},\boldsymbol{y})$ are in principle $\boldsymbol{y}$-dependent with non-vanishing divergence. Under the assumption that (4.2) holds, formula (3.10) for the effective permittivity simply reduces to

$$\varepsilon^{\mathrm{eff}}=\int_Y\varepsilon(\boldsymbol{x},\boldsymbol{y})\,\mathrm{d}y-\frac{1}{i\omega}\int_\Sigma\sigma(\boldsymbol{x},\boldsymbol{y})\,\mathrm{d}o_y-\frac{1}{i\omega}\int_{\partial\Sigma\setminus\partial Y}\lambda(\boldsymbol{x},\boldsymbol{y})\,\mathrm{d}s\;. \tag{4.3}$$

By this simplified (geometric) average, one may directly influence the effective permittivity tensor by either adjusting the operating frequency, ω, or by tuning the parameters $\sigma(\boldsymbol{x},\boldsymbol{y})$ and $\lambda(\boldsymbol{x},\boldsymbol{y})$.

We add a remark on the above formalism. A natural question at this point concerns the existence of suitable configurations that obey (4.2). More precisely, it is of interest to specify configurations that allow for a vanishing corrector while two or all three of the distinct averages in (4.3) are nonzero. We give three related examples here. First, consider the geometry consisting of parallel, planar sheets with constant σ and no edges, $\partial\Sigma=\emptyset$, embedded in a homogeneous dielectric host with uniform ε; see Figure 3a. In this case, $\boldsymbol{\chi}\equiv 0$, and we can have a nonzero contribution from the average of σ in (4.3). The second geometry consists of parallel and periodically aligned nanoribbons embedded in a homogeneous, dielectric host; see Figure 3b. In this case, we can achieve $\boldsymbol{\chi}\equiv 0$ through (4.2) and a nonzero contribution of the line average of λ in (4.3) by setting $\sigma^d=0$ and choosing a constant λ^d. Further, in the same geometry, by choosing a constant σ and the y_3-dependent line conductivity $\lambda=\sigma\,y_3$, all three averages in (4.3) are nonzero while condition (4.2) holds; thus, $\boldsymbol{\chi}\equiv 0$. An example with a geometry that always has a nonzero corrector (in the presence of a nonzero conductivity σ) consists of parallel and periodically aligned nanotubes; see Figure 3c.

4.2. Vanishing corrector: A notion of critical spacing. In this subsection, we further simplify average (4.3) in order to derive an explicit formula for the critical spacing, d_c. Recall the ansatz

$$\sigma^d(\boldsymbol{x}) = d\,\sigma(\boldsymbol{x}, \boldsymbol{x}/d), \quad \lambda^d(\boldsymbol{x}) = d^2\,\lambda(\boldsymbol{x}, \boldsymbol{x}/d)\ ;$$

see Section 1 2.1. Although this choice of scaling is convenient for the asymptotic analysis (Section 3), it introduces two parameters, σ and λ, that couple the physical conductivities, σ^d and λ^d, with the spacing, d. This coupling may obscure the physical insight possibly gained by the averaging in (4.3). A reason is that, in realistic settings, the parameters d, σ^d and λ^d are controlled independently by tuning of the geometry and the electronic structure of the 2D material [23].

As a remedy, consider the following rescaled quantities

$$\sigma^d(\boldsymbol{x}, \boldsymbol{y}) := d\,\sigma(\boldsymbol{x}, \boldsymbol{y})\ , \quad \lambda^d(\boldsymbol{x}, \boldsymbol{y}) := d^2\,\lambda(\boldsymbol{x}, \boldsymbol{y})\ ,$$

where the microscale variable, y, is singled out and treated as independent in the actual conductivities, $\sigma^d(\boldsymbol{x})$ and $\lambda^d(\boldsymbol{x})$. The averages of interest therefore are

$$\bar{\varepsilon}\,(\boldsymbol{x}) = \int_Y \varepsilon\,(\boldsymbol{x}, \boldsymbol{y})\,\mathrm{d}y\ , \quad \bar{\sigma}^d(\boldsymbol{x}) = \int_\Sigma \sigma^d(\boldsymbol{x}, \boldsymbol{y})\,\mathrm{d}o_y\ , \quad \bar{\lambda}^d(\boldsymbol{x}) = \int_{\partial\Sigma\setminus\partial Y} \lambda^d(\boldsymbol{x}, \boldsymbol{y})\,\mathrm{d}s\ .$$

For slowly varying parameters, these averages simply reduce to the original parameters. We assume that $\bar{\varepsilon}\,(\boldsymbol{x})$, $\bar{\sigma}^d(\boldsymbol{x})$ and $\bar{\lambda}^d(\boldsymbol{x})$ have the same eigenvectors, or *principal axes*, $\boldsymbol{r}_i$ $(i = 1, 2, 3)$. Let $\bar{\varepsilon}_i$, $\bar{\sigma}^d_i$, and $\bar{\lambda}^d_i$, denote the corresponding eigenvalues of the averaged tensors. (Only two eigenvalues of $\bar{\sigma}^d$ and one eigenvalue of $\bar{\lambda}^d$ are possibly nonzero.) After some algebra, (4.3) gives

$$\frac{\varepsilon^{\mathrm{eff}}_i}{\bar{\varepsilon}_i} \;=\; \Big(1 - \frac{\xi_{0,i}}{d}\Big)\Big(1 + \frac{\bar{\lambda}^d_i}{i\omega\bar{\varepsilon}_i\,\xi_{0,i}\,d}\Big)\ , \tag{4.4}$$

for all directions $\boldsymbol{r}_i$ with nonzero $\bar{\sigma}^d_i$, or $\bar{\lambda}^d_i$. Here, we define the *generalized plasmonic thickness* [21]

$$\xi_{0,i} \;=\; \frac{\bar{\sigma}^d_i}{2\,i\omega\bar{\varepsilon}_i} + \sqrt{\Big(\frac{\bar{\sigma}^d_i}{2\,i\omega\bar{\varepsilon}_i}\Big)^2 + \frac{\bar{\lambda}^d_i}{i\omega\bar{\varepsilon}_i}}\ , \tag{4.5}$$

which accounts for the line conductivity. Evidently, $\varepsilon^{\mathrm{eff}}_i \simeq 0$ if the spacing, d, is close to the critical value $d_c = \xi_{0,i}$ for some i and suitable ranges of values for $\bar{\sigma}^d_i$ and $\bar{\lambda}^d_i$ (e.g., $\operatorname{Im}\bar{\sigma}^d_i > 0, \operatorname{Im}\bar{\lambda}^d_i > 0$).

We stress that for $|\bar{\sigma}^d_i| \gg |\bar{\lambda}^d_i|$ (4.4) with (4.5) reduces to the known result

$$\frac{\varepsilon^{\mathrm{eff}}_i}{\bar{\varepsilon}_i} \;\sim\; \Big(1 - \frac{\xi_{0,i}}{d}\Big)\ , \qquad \xi_{0,i} \;\approx\; \frac{\bar{\sigma}^d_i}{i\omega\bar{\varepsilon}_i}\ ,$$

which is also obtained via a Bloch-wave approach for planar sheets [21]. In contrast, if $|\bar{\lambda}^d_i| \gg |\bar{\sigma}^d_i|$, (4.4) reduces to

$$\frac{\varepsilon^{\mathrm{eff}}_i}{\bar{\varepsilon}_i} \;\sim\; \Big(1 - \frac{\xi_{0,i}}{d}\Big)\ , \qquad \xi_{0,i} \;\approx\; \sqrt{\frac{\bar{\lambda}^d_i}{i\omega\bar{\varepsilon}_i}}.$$

Notice the distinctly different scaling of $\xi_{0,i}$ with the conductivity parameter in this regime.

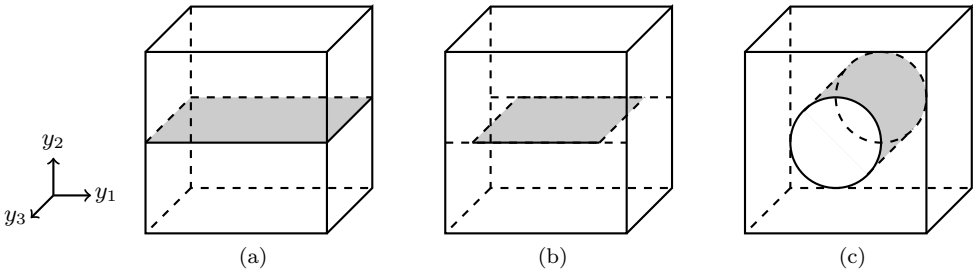

Fig. 3: Prototypical examples of microscopic geometries with conducting sheets for cell problem (3.8). (a) Infinite planar sheet, with no edges. (b) Planar strip (nanoribbon). (c) Sheet forming circular cylinder (nanotube). The corrector, $\boldsymbol{\chi}$, can be characterized as follows: (a) $\boldsymbol{\chi} \equiv 0$; (b) $\chi_2 = \chi_3 \equiv 0$ while χ_1 is nontrivial; and (c) $\chi_3 \equiv 0$ while χ_1 and χ_2 are nontrivial.

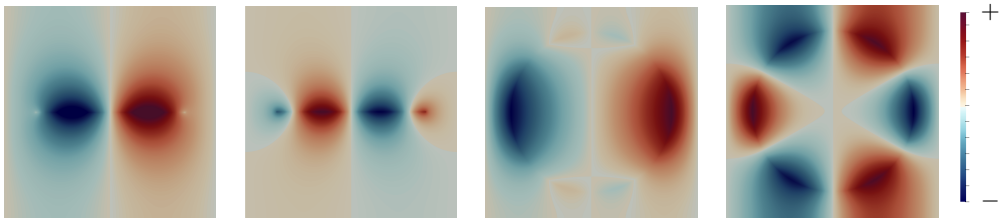

(a) $\operatorname{Re}\chi_1$, ribbons (b) $\operatorname{Im}\chi_1$, ribbons (c) $\operatorname{Re}\chi_1$, tubes (d) $\operatorname{Im}\chi_1$, tubes

Fig. 4: Real and imaginary parts of corrector component χ_1 for geometries of Figures 3b,c in y_1y_2-plane. It is evident that internal edges in nanoribbons and curvature in nanotubes create SPPs.

4.3. On the physical role of corrector $\boldsymbol{\chi}$. Let us return to cell problem (3.8). We now provide a physical interpretation of its solution, the corrector $\boldsymbol{\chi}$. In particular, we solve cell problem (3.8) for the three prototypical configurations shown in Figure 3 (see also Section 4 4.1). In all three geometries, we set the permittivity and surface conductivity equal to nonzero constants, $\varepsilon(\boldsymbol{x}, \boldsymbol{y}) = \varepsilon$, $\sigma(\boldsymbol{x}, \boldsymbol{y}) = \sigma$, while we take $\lambda(\boldsymbol{x}, \boldsymbol{y}) = 0$. By the discussion in Section 4 4.1, we conclude that for the geometry of planar sheets with no edges (Figure 3(a)) $\boldsymbol{\chi} \equiv 0$. For the geometry of nanoribbons (Figure 3(b)), $\chi_2 \equiv \chi_3 \equiv 0$. The remaining geometry (Figure 3(c)) has only one vanishing corrector component, $\chi_3 \equiv 0$. The real and imaginary parts of the nontrivial corrector component χ_1 for the last two geometries are shown in Figure 4. The SPP excited by the edge discontinuity is evident in these settings; cf. [19].

Motivated by these numerical results, we develop an argument that the corrector, $\boldsymbol{\chi}$, encodes the microscale response of the system to the macroscopic electromagnetic field, $(\boldsymbol{\mathcal{E}}(\boldsymbol{x}), \boldsymbol{\mathcal{H}}(\boldsymbol{x}))$. We start by noting that our scalings $\sigma^d(\boldsymbol{x}) = d\,\sigma(\boldsymbol{x}, \boldsymbol{x}/d)$ and $\lambda^d(\boldsymbol{x}) = d^2\,\lambda(\boldsymbol{x}, \boldsymbol{x}/d)$ imply that the typical length scales of surface and line waves (such as SPPs and EPPs) scale with d and d^2, respectively. Accordingly, we can identify the forcing in cell problem (3.8) due to $\boldsymbol{e}_j$; it corresponds to a (normalized)

asymptotically slow planar wave. In this sense, the cell problem describes the *local response of the microstructure* to all possible excitations by local plane waves.

This interpretation has an important consequence in light of the discussion in Section 4 4.1: All cases of vanishing correctors are indeed characterized by conditions (4.2). In fact, conditions (4.2) characterize exactly all microscale geometries that *do not permit* the excitation of SPPs by plane waves.

5. Numerical results: Effective permittivity and Lorentz resonance. In this section, we present a number of computational results concerning the effective permittivity computed from (3.10) by use of cell problem (3.8). We also compute the (effective) macroscale electric field. We present results for geometries depicted in Figure 3. We construct a Lorentzian function that describes the effective permittivity tensor as a function of frequency.

5.1. Drude model and rescaling. In order to relate numerical results obtained by solving cell problem (3.8) to the averaging in (3.10) and compute physical quantities as a function of frequency, ω, it is necessary to use suitable models for the material parameters. If $\lambda^d = 0$, the only modeling parameters that enter (3.8) are $\varepsilon(\boldsymbol{x}, \boldsymbol{y})$ and $\frac{1}{i\omega}\sigma(\boldsymbol{x}, \boldsymbol{y})$. We will assume that $\varepsilon(\boldsymbol{x}, \boldsymbol{y}) = \varepsilon$ is constant and that the tangential parts of $\sigma(\boldsymbol{x}, \boldsymbol{y}) = \sigma(\boldsymbol{y})$ are given by spatially constant values. Thus, the only microscale ($\boldsymbol{y}$-) parameter dependence to be accounted for is the one in $\frac{1}{i\omega}\sigma(\boldsymbol{x}, \boldsymbol{y})$; cf. Figure 3.

The surface conductivity, σ^d, of doped graphene can plausibly be described by the Kubo formula, which takes into account electronic excitations and temperature effects [6]. However, in the terahertz frequency regime, in which fine-scale SPPs on graphene are typically generated, it is reasonable to simplify this description to the (primarily phenomenological) Drude model [6, 11, 23]. By this model, the tangential components of a spatially constant σ^d are

$$\sigma^d = \frac{i\, e^2\, E_F}{\varepsilon_0\, \pi\hbar^2\, \big(\omega + i/\tau\big)} \ .$$

Here, e is the electron charge; $\hbar$ denotes the (reduced) Planck constant; ε_0 is the vacuum permittivity; E_F denotes the Fermi energy; and τ is the electronic relaxation time. In this context, an $\boldsymbol{x}$-dependence of σ^d may arise from spatial variations of the parameters E_F and τ.

In view of the typical parameter values for graphene [6], we use $\tau = 0.5\,10^{-12}$s and the following rescalings:

$$E_F \ = \ \tilde{E}_F\, 10^{-19}\mathrm{J}, \qquad \omega \ = \ \tilde{\omega}\, 10^{14}\mathrm{Hz}, \qquad d \ = \ \tilde{d}\, 10\,\mathrm{nm},$$

with $0 \le \tilde{E}_F \le 1.6$, $0.5 \le \tilde{\omega} \le 4.0$, and $0 \le \tilde{d} \le 20.0$. In this vein, the surface average in (3.10) of the effective permittivity tensor, $\varepsilon^{\mathrm{eff}}$, has the constant ($\boldsymbol{y}$-independent) prefactor

$$\eta := \frac{1}{i\omega}\,\sigma \ = \ \frac{1}{i\omega\, d}\,\sigma^d \ = \ 82.9\,\frac{\tilde{E}_F}{\tilde{d}\,\tilde{\omega}\,\big(\tilde{\omega} + 0.02\, i\big)} \ . \tag{5.1}$$

Utilizing definition (5.1) we conveniently express the matrix elements of $\varepsilon^{\mathrm{eff}}$ given in (3.10) as

$$\frac{\varepsilon^{\mathrm{eff}}_{ij}}{\varepsilon} = 1 \ - \ \frac{\eta}{\varepsilon} \int_\Sigma P_t(\boldsymbol{y})\big(\boldsymbol{e}_j + \nabla_y \chi_j(\boldsymbol{x}, \boldsymbol{y})\big) \cdot \boldsymbol{e}_i \, \mathrm{d}o_y \ .$$

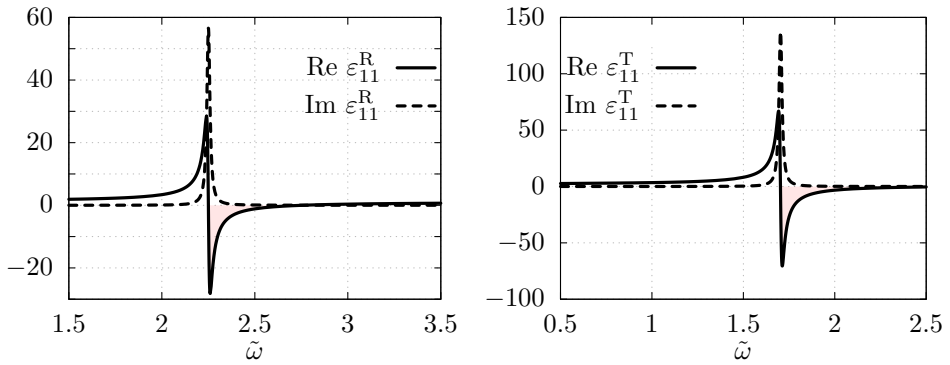

(a) (b)

Fig. 5: Plots of real and imaginary parts of matrix elements of ε^{eff} as a function of frequency by (5.2) for the geometries of Figures 3b, c. (a) $\varepsilon^{\mathrm{R}}_{11}$ for nanoribbons; and (b) $\varepsilon^{\mathrm{T}}_{11}$ or $\varepsilon^{\mathrm{T}}_{22}$ ($\varepsilon^{\mathrm{T}}_{11} = \varepsilon^{\mathrm{T}}_{22}$) for nanotubes. The shaded area indicates the frequency regime for negative real part in each case.

Here, $P_t(\boldsymbol{y})$ denotes the projection onto the tangential space of Σ^d at point $\boldsymbol{y}$. This formula for $\varepsilon^{\text{eff}}_{ij}$ uncovers an important property: Up to a factor of ε, computational results for the cell problem only depend on the ratio η/ε. Thus, it is sufficient to compute values for $\varepsilon^{\text{eff}}_{ij}$ by setting $\varepsilon = 1$.

5.2. Effective permittivity tensors in prototypical geometries. Let us now recall the discussion about vanishing correctors in Sections 4 4.1,4.3. For the prototypical geometries of Figure 3, the respective effective permittivities have the matrix forms

(5.2)
$$\varepsilon^{\text{eff}}_{\mathrm{S}} = \begin{pmatrix} \varepsilon^{\mathrm{S}}_{11} & 0 & 0 \\ 0 & \varepsilon & 0 \\ 0 & 0 & \varepsilon^{\mathrm{S}}_{33} \end{pmatrix}, \qquad \varepsilon^{\text{eff}}_{\mathrm{R}} = \begin{pmatrix} \varepsilon^{\mathrm{R}}_{11} & 0 & 0 \\ 0 & \varepsilon & 0 \\ 0 & 0 & \varepsilon^{\mathrm{R}}_{33} \end{pmatrix}, \qquad \varepsilon^{\text{eff}}_{\mathrm{T}} = \begin{pmatrix} \varepsilon^{\mathrm{T}}_{11} & 0 & 0 \\ 0 & \varepsilon^{\mathrm{T}}_{22} & 0 \\ 0 & 0 & \varepsilon^{\mathrm{T}}_{33} \end{pmatrix}.$$

Here, the subscript (S, R or T) for each matrix indicates the type of geometry: S corresponds to the geometry with planar sheets and no edges (Figure 3a); R stands for the nanoribbons geometry (Figure 3b); and T corresponds to the nanotubes geometry (Figure 3c). Due to vanishing corrector components, the matrix element $\varepsilon^{\mathrm{S}}_{11}$ is given in closed form by (4.3), viz.,

(5.3)
$$\varepsilon^{\mathrm{S}}_{11} = 1 - \eta\,; \quad \varepsilon^{\mathrm{S}}_{11} = \varepsilon^{\mathrm{S}}_{33} = \varepsilon^{\mathrm{R}}_{33} = \varepsilon^{\mathrm{T}}_{33}\,.$$

In the numerical computations of this section, we focus on the geometries with nanoribbons and nanotubes. To determine $\varepsilon^{\mathrm{R}}_{11}$ and $\varepsilon^{\mathrm{T}}_{11} = \varepsilon^{\mathrm{T}}_{22}$, we solve cell problem (3.8) directly and compute the average by (3.10). The computations are carried out by the finite element toolkit deal.II [4]. To this end, we sample over the frequency range $0.5 \le \tilde{\omega} \le 4.0$ with the choice $\tilde{E}_F = 1$ and $\tilde{d} = 20.72$. The real and imaginary parts of $\varepsilon^{\mathrm{R}}_{11}$ and $\varepsilon^{\mathrm{T}}_{11}$ are plotted as a function of frequency in Figures 5a, b. We observe that each of these functions exhibits a strong resonance.

In view of these results, it is compelling to describe the behavior of ε^{eff} as a function of ω by a Lorentzian function. More precisely, to quantify the observed resonances, we fit the model

$$\varepsilon(\tilde{\omega}) = \varepsilon_\infty + \frac{f\,\tilde{\omega}_R^2}{\tilde{\omega}^2 - \tilde{\omega}_R^2 + i\tilde{\Gamma}\,\tilde{\omega}}$$

onto the numerical results (Figures 5a, b). The real and imaginary parts of this ε satisfy the Kramers-Kronig relations. We achieve an excellent agreement of the fitting curve and the numerically computed values with the following set of parameters:

$$\begin{aligned}
\varepsilon_{11}^{\text{R}}:&\ \ \tilde{\omega}_R = 2.25002(2)\ ,\quad \tilde{\Gamma} = 0.02001(7)\ ,\quad \varepsilon_\infty = 0.90(2)\ ,\quad f = -0.503(2)\ ,\\
\varepsilon_{11}^{\text{T}}:&\ \ \tilde{\omega}_R = 1.70285(3)\ ,\quad \tilde{\Gamma} = 0.02000(7)\ ,\quad \varepsilon_\infty = 0.43(5)\ ,\quad f = -1.614(4)\ .
\end{aligned}$$

It is of interest to note that the ENZ effect occurs at the following (rescaled) frequencies:

$$\varepsilon_{11}^{\text{R}}:\ \ \tilde{\omega} \approx 2.752\ ,\qquad \varepsilon_{11}^{\text{T}}:\ \ \tilde{\omega} \approx 2.755\ .$$

Here, both frequencies were determined by interpolating the numerical result displayed in Figure 5 and equating the real part to zero. Furthermore, (5.3) implies the critical frequency $\tilde{\omega} \approx 2$ for $\varepsilon_{11}^{\text{S}}$ where $\varepsilon_{11}^{\text{S}} = \varepsilon_{33}^{\text{S}} = \varepsilon_{33}^{\text{R}} = \varepsilon_{33}^{\text{T}}$.

5.3. Results on homogenized system. Next, we present computational results for the macroscopic electric field, $\boldsymbol{\mathcal{E}}(\boldsymbol{x})$, by solving (3.12). We use the scattering configuration of Figure 2, but replace the periodic microstructure by a slab with a uniform permittivity tensor ε^{eff} given by (5.2). As indicated in Figure 2, we perform 2D simulations in the x_1x_2-plane with an electric Hertzian dipole source, oriented in the x_2-direction and located underneath the slab. We assume that the incident wave is TM polarized, and the whole structure is translation invariant in the x_3-direction; see also [21]. Figures 6 and 7 show results for the geometries with nanoribbons and nanotubes, respectively. By tuning the parameter η, we observe usual propagation in all directions (Figure 6a, d, Figure 7a, d), the ENZ effect (one eigenvalue of ε^{eff} is close to zero, Figure 6b, e, Figure 7b, e), hyperbolic propagation (both eigenvalues of ε^{eff} have opposite signs, Figure 6c, f), and propagation in metallic regime (both eigenvalues of ε^{eff} are negative, Figure 7c, f).

6. Conclusion. In this paper, we carried out a formal asymptotic analysis to homogenize time-harmonic Maxwell's in plasmonic crystals made of conducting sheets with microscale spacing d, in the limit as $d \to 0$ via suitable scalings of material parameters. The homogenized system features an effective permittivity tensor, ε^{eff}, given by an averaging procedure that involves a weighted volume average of the bulk permittivity, as well as a weighted surface average of the surface conductivity, σ^d, and a weighted line average of the line charge density, λ^d, of the sheets. The vector-valued corrector field of this procedure solves a closed cell problem. We showed analytically how the combination of the complex-valued σ^d and λ^d yields an ENZ effect; and defined the related critical spacing which depends on σ^d and λ^d. Further, we demonstrated numerically distinct behaviors of the macroscale electric field; and how resonances for the effective permittivity in different geometries can be viewed as universal Lorentz-type resonances.

Our results have a few limitations and point to open problems. For instance, the asymptotic analysis is based on a strong periodicity assumption for the microstructure. Further, we do not discuss boundary layers in the homogenization procedure due to

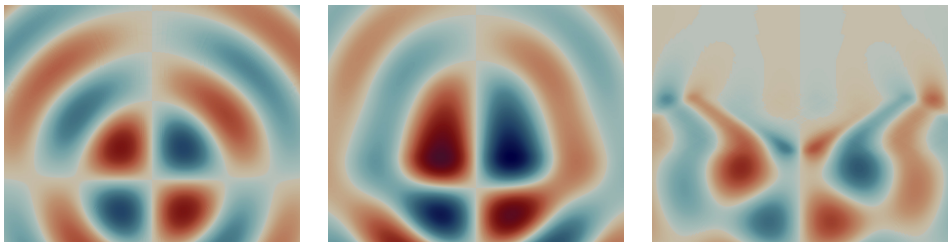

(a) $\operatorname{Re}\mathcal{E}_1$ for $\operatorname{Re}\varepsilon_{11}^{\mathrm{R}} > 0$ (b) $\operatorname{Re}\mathcal{E}_1$ for $\operatorname{Re}\varepsilon_{11}^{\mathrm{R}} \approx 0$ (c) $\operatorname{Re}\mathcal{E}_1$ for $\operatorname{Re}\varepsilon_{11}^{\mathrm{R}} < 0$

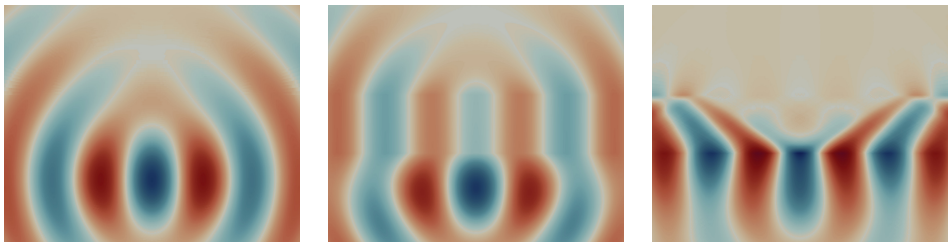

(d) $\operatorname{Re}\mathcal{E}_2$ for $\operatorname{Re}\varepsilon_{11}^{\mathrm{R}} > 0$ (e) $\operatorname{Re}\mathcal{E}_2$ for $\operatorname{Re}\varepsilon_{11}^{\mathrm{R}} \approx 0$ (f) $\operatorname{Re}\mathcal{E}_2$ for $\operatorname{Re}\varepsilon_{11}^{\mathrm{R}} < 0$

Fig. 6: Numerical simulations for real parts of x_1- and x_2-components of macroscale electric field, $\boldsymbol{\mathcal{E}}(\boldsymbol{x})$, in scattering geometry of Figure 2 with unit cell containing nanoribbon (Figure 3(b)). Plots indicate three distinct behaviors: Usual propagation ($\operatorname{Re}\varepsilon_{11}^{\mathrm{R}} > 0$) [(a),(d)]; propagation with ENZ effect ($\operatorname{Re}\varepsilon_{11}^{\mathrm{R}} \approx 0$) [(b),(e)]; and propagation in hyperbolic regime ($\operatorname{Re}\varepsilon_{11}^{\mathrm{R}} < 0$) [(c),(f)].

the interaction of the microstructure with boundaries of the (scattering) domain. It is also worth mentioning that scaling assumptions different from the ones chosen here may lead to different homogenization results.

Acknowledgments. We acknowledge support by ARO MURI Award W911NF-14-0247 (MMai, MMat, EK, ML, DM); EFRI 2-DARE NSF Grant 1542807 (MMat); and NSF DMS-1412769 (DM).

REFERENCES

[1] A. Alù and N. Engheta, *Achieving transparency with plasmonic and metamaterial coatings*, Phys. Rev. E, 72 (2005), p. 016623.

[2] Y. Amirat and V. V. Shelukhin, *Homogenization of the time harmonic Maxwell equations and the frequency dispersion effect*, Journal de Mathématiques Pures et Appliquées, 95 (2011), pp. 420–443.

[3] Y. Amirat and V. V. Shelukhin, *Homogenization of time harmonic Maxwell equations: the effect of interfacial currents*, Mathematical Methods in the Applied Sciences, 40 (2017), pp. 3140–3162.

[4] D. Arndt, W. Bangerth, D. Davydov, T. Heister, L. Heltai, M. Kronbichler, M. Maier, B. Turcksin, and D. Wells, *The deal.II Library, Version 8.5*, Journal of Numerical Mathematics, 25 (2017), pp. 137–145.

[5] A. Bensoussan, J.-L. Lions, and G. Papanicolaou, *Asymptotic analysis for periodic structures*, vol. 5 of Studies in Mathematics and its Applications, North-Holland, 1st ed., 1978.

[6] Y. V. Bludov, A. Ferreira, N. M. R. Peres, and M. I. Vasilevskiy, *A primer on surface plasmon-polaritons in graphene*, International Journal on Modern Physics B, 27 (2013), p. 1341001.

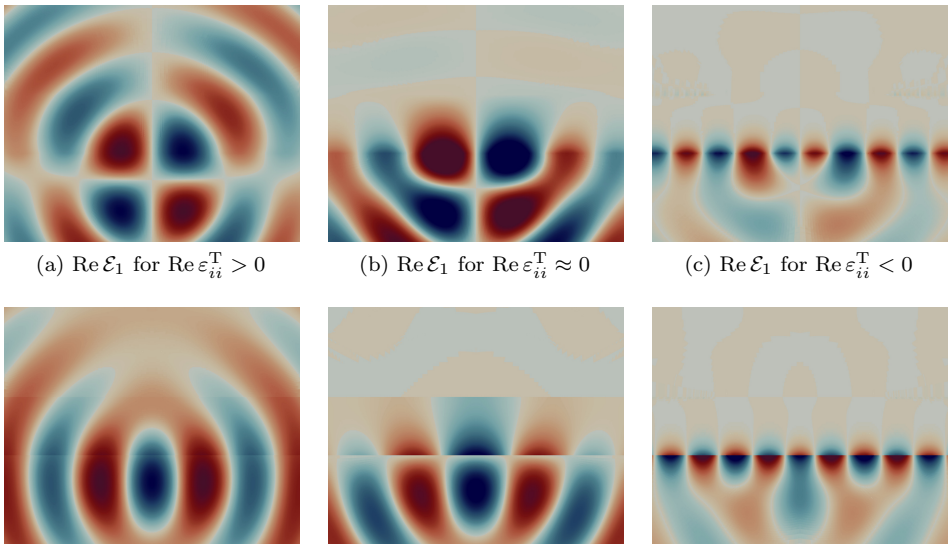

(a) $\operatorname{Re}\mathcal{E}_1$ for $\operatorname{Re}\varepsilon_{ii}^{\mathrm{T}} > 0$ (b) $\operatorname{Re}\mathcal{E}_1$ for $\operatorname{Re}\varepsilon_{ii}^{\mathrm{T}} \approx 0$ (c) $\operatorname{Re}\mathcal{E}_1$ for $\operatorname{Re}\varepsilon_{ii}^{\mathrm{T}} < 0$

(d) $\operatorname{Re}\mathcal{E}_2$ for $\operatorname{Re}\varepsilon_{ii}^{\mathrm{T}} > 0$ (e) $\operatorname{Re}\mathcal{E}_2$ for $\operatorname{Re}\varepsilon_{ii}^{\mathrm{T}} \approx 0$ (f) $\operatorname{Re}\mathcal{E}_2$ for $\operatorname{Re}\varepsilon_{ii}^{\mathrm{T}} < 0$

Fig. 7: Numerical simulations for real parts of x_1- and x_2- components of macroscale electric field, $\boldsymbol{\mathcal{E}}(\boldsymbol{x})$, in the scattering geometry of Figure 2 with unit cell containing nanotube (Figure 3(c)). The plots indicate three distinct behaviors: Usual propagation ($\operatorname{Re}\varepsilon_{ii}^{\mathrm{T}} > 0$) [(a),(d)]; propagation with ENZ effect ($\operatorname{Re}\varepsilon_{ii}^{\mathrm{T}} \approx 0$) [(b),(e)]; and propagation in metallic regime ($\operatorname{Re}\varepsilon_{ii}^{\mathrm{T}} < 0$) [(c),(f)].

[7] G. Bouchitté and B. Schweizer, *Homogenization of maxwell's equations in a split ring geometry*, Multiscale Modeling & Simulation, 8 (2010), pp. 717–750.

[8] C. Caloz, A. Lai, and T. Itoh, *The challenge of homogenization in metamaterials*, New Journal of Physics, 7 (2005), pp. 167/1–15.

[9] J. Cheng, W. L. Wang, H. Mosallaei, and E. Kaxiras, *Surface plasmon engineering in graphene functionalized with organic molecules: A multiscale theoretical investigation*, Nano Letters, 14 (2014), pp. 50–56.

[10] Z. Fei, M. D. Goldflann, J.-S. Wu, M. Wagner, A. S. McLoed, M. K. Liu, K. W. Post, S. Zhu, G. C. A. M. Janssen, M. M. Fogler, and D. N. Basov, *Edge and surface plasmons in graphene nanoribbons*, Nano Letters, 15, pp. 8271–8276.

[11] A. N. Grigorenko, M. Polini, and K. S. Novoselov, *Graphene plasmonics*, Nature Photonics, 6 (2012), pp. 749–758.

[12] S. Guenneau, F. Zolla, and A. Nicolet, *Homogenization of 3d finite photonic crystals with heterogeneous permittivity and permeability*, Waves in Random and Complex Media, 17 (2007), pp. 653–697.

[13] X. Huang, Y. Lai, Z. H. Hang, H. Zheng, and C. T. Chan, *Dirac cones induced by accidental degeneracy in photonic crystals and zero-refractive-index materials*, Nat. Mater., 10 (2011), pp. 582–586.

[14] S. Jahani and Z. Jacob, *All-dielectric metamaterials*, Nature Nanotechnology, 11 (2016), pp. 23–36.

[15] G. Kirstensson, *Homogenization of corrugated interfaces in electromagnetics*, Progress in Electromagnetics Research, 55 (2005), pp. 1–31.

[16] J. R. Krenn and J.-C. Weeber, *Surface plasmon polaritons in metal stripes and wires*, Philosophical Transcations of the Royal Society A, 362 (2004), pp. 739–756.

[17] P. Lalanne, *Effective medium theory applied to photonic crystals composed of cubic or square cylinders*, Applied Optics, 35 (1996), pp. 5369–5380.

[18] T. Low, A. Chaves, J. D. Caldwell, A. Kumar, N. X. Fang, P. Avouris, T. F. Heinz, F. Guinea, L. Martin-Moreno, and F. Koppens, *Polaritons in*

layered two-dimensional materials, Nature Materials, 16 (2017), pp. 182–194.
[19] M. Maier, D. Margetis, and M. Luskin, *Generation of surface plasmon-polaritons by edge effects*, Communications in Mathematical Sciences, 16 (2018), pp. 77–95.
[20] M. Maier, D. Margetis, and A. Mellet, *Homogenization of Maxwell's equations in nonhomogeneous plasmonic structures*, Submitted, (2018). Preprint at arXiv:1805.07671 [math.AP].
[21] M. Maier, M. Mattheakis, E. Kaxiras, M. Luskin, and D. Margetis, *Universal behavior of dispersive Dirac cone in gradient-index plasmonic metamaterials*, Physical Review B, 97 (2018).
[22] S. A. Maier, *Plasmonics: Fundamentals and applications*, Springer, New York, 2007.
[23] M. Mattheakis, C. A. Valagiannopoulos, and E. Kaxiras, *Epsilon-near-zero behavior from plasmonic dirac point: Theory and realization using two-dimensional materials*, Physical Review B, 94 (2016), p. 201404(R).
[24] P. Moitra, Y. Yang, Z. Anderson, I. I. Kravchenko, D. P. Briggs, and J. Valentine, *Realization of an all-dielectric zero-index optical metamaterial*, Nature Photonics, 7 (2013), pp. 791–795.
[25] C. Müller, *Foundations of the mathematical theory of electromagnetic waves*, Springer-Verlag, New York, 1969.
[26] A. Nemilentsau, T. Low, and G. Hanson, *Anisotropic 2d materials for tunable hyperbolic plasmonics*, Phys. Rev. Lett., 116 (2016), p. 066804.
[27] J. Nevard and J. B. Keller, *Homogenization of rough boundaries and interfaces*, SIAM Journal of Applied Mathematics, 57 (1997), pp. 1660–1686.
[28] X. Niu, X. Hu, S. Chu, and Q. Gong, *Epsilon-near-zero photonics: A new platform for integrated devices*, Adv. Optical Mater., 6 (2018), p. 1701292.
[29] G. T. Papadakis, D. Fleischman, A. Davoyan, P. Yeh, and H. A. Atwater, *Optical magnetism in planar metamaterial heterostructures*, Nature Communications, 9 (2018), p. 296.
[30] G. Pavliotis and A. Stuart, *Multiscale methods: Averaging and homogenization*, Springer, 2007.
[31] V. V. Shelukhin and S. A. Terentev, *Frequency dispersion of dielectric permittivity and electric conductivity of rocks via two-scale homogenization of the Maxwell equations*, Progress in Electromagnetics Research B, 14 (2009), pp. 175–202.
[32] S. N. Shirodkar, M. Mattheakis, P. Cazeaux, P. Narang, M. Soljačić, and E. Kaxiras, *Quantum plasmons with optical-range frequencies in doped few-layer graphene*, Phys. Rev. B, 97 (2018), p. 195435.
[33] M. Silveirinha and N. Engheta, *Tunneling of electromagnetic energy through subwavelength channels and bends using epsilon-near-zero materials*, Phus. Rev. Lett., 97 (2006), p. 157403.
[34] D. Sjöberg, C. Engström, G. Kristensson, D. J. N. Wall, and N. Wellander, *A Floquet-Bloch decomposition of Maxwell's equations applied to homogenization*, SIAM Multiscale Modeling and Simulation, 4 (2005), pp. 149–171.
[35] N. Wellander and G. Kristensson, *Homogenization of the Maxwell equations at fixed frequency*, SIAM Journal on Applied Mathematics, 64 (2003), pp. 170–195.
[36] D. Wintz, P. Genevet, A. Ambrosio, A. Woolf, and F. Capasso, *Holographic metalens for switchable focusing of surface plasmons*, Nano Letters, 15 (2015), pp. 3585–3589.
[37] F. Xia, H. Wang, D. Xiao, M. Dubey, and A. Ramasubramaniam, *Two-dimensional material nanophotonics*, Nat. Photon, 8 (2014), pp. 899–907.
[38] N. I. Zheludev and E. Plum, *Reconfigurable nanomechanical photonic metamaterials*, Nature Nanotechnology, 11 (2016), pp. 16–22.